Hot-casting assisted liquid additive engineering for efficient and stable perovskite solar cells

Hanul Min[1,2,*], Junnan Hu[1], Zhaojian Xu[1], Tianran Liu[1], Saeed-Uz-Zaman Khan[1], Kwangdong Roh[1,3], Yueh-Lin Loo[4], Barry P. Rand[1,5,*]

[1]Department of Electrical and Computer Engineering, Princeton University, Princeton, New Jersey 08544, United States

[2]Princeton Institute for International and Regional Studies, Princeton University, Princeton, New Jersey 08544, United States

[3]Present address: Department of Physics, Ewha Womans University, Seoul 03760, Republic of Korea

[4]Department of Chemical and Biological Engineering, Princeton University, Princeton, New Jersey 08544, United States

[5]Andlinger Center for Energy and the Environment, Princeton University, Princeton, New Jersey 08544, United States

*To whom correspondence should be addressed. E-mail: hm0460@princeton.edu; brand@princeton.edu

Abstract:

High-performance inorganic-organic lead halide perovskite solar cells (PSCs) are often fabricated with a liquid additive such as dimethyl sulfoxide (DMSO) which retards crystallization and reduces roughness and pinholes in the perovskite layers. However, DMSO can be trapped during perovskite film formation and induce voids and undesired reaction byproducts upon later processing steps. Here, we show that we can reduce the amount of residual DMSO in as-spin-coated films significantly - by 30 times - through use of pre-heated

substrates, or a so-called hot-casting method. Hot-casting increases the perovskite film thickness given the same concentration of solutions which allows us to reduce the perovskite solution concentration. By reducing the amount of DMSO in proportion to the concentration of perovskite precursors and using hot-casting, we are able to fabricate perovskite layers with improved perovskite-substrate interfaces by suppressing the formation of byproducts which increase trap density and accelerate degradation of the perovskite layers. The best-performing PSCs exhibit power conversion efficiency (PCE) of 23.4% (23.0% stabilized efficiency) under simulated solar illumination. Furthermore, encapsulated devices showed considerably reduced post-burn-in decay of -0.84% of initial efficiency per 100 h, retaining more than 80% and 93% of their initial and post-burn-in efficiencies after 800 h of operation with maximum power point tracking (MPPT) under high-power of ultraviolet-(UV-)containing continuous light exposure (overall power density of 1.1 sun with 2.6 times higher UV-region power density than AM 1.5G).

Main text:

Mixed solvent systems comprising a main solvent (e.g., *N,N*-dimethylformamide (DMF), 2-methoxyethanol (2-ME), or γ-butyrolactone (GBL)) and a secondary solvent or additive (e.g., dimethyl sulfoxide (DMSO) or *N*-methyl-2-pyrrolidone (NMP)) are common practice in inorganic-organic hybrid metal halide perovskite precursor inks. The role of the secondary solvent or additive is understood as retarding the crystallization process, but is also often complicated and suffers from coordination with perovskite precursors.[1] A combination of these solvents such as GBL/DMSO,[1-2] DMF/NMP,[3-4] 2-ME/DMSO,[5] and DMF/DMSO[6-7] have been adopted in a wide variety of ways depending on the composition of the perovskite or the coating method. Among various blends of solvents and perovskite precursors,

DMF/DMSO containing formamidinium lead iodide (FAPbI$_3$) with a small amount of α-phase stabilizer have recently shown the ability to fabricate efficient single-junction perovskite solar cells (PSCs) with efficiencies greater than 24%.[8-14] However, DMSO, with a relatively high boiling point and strong coordination, can be trapped during film formation and accelerate the degradation of the resulting films.[15] Furthermore, DMSO, a Lewis-base solvent, can initiate deprotonation of organic cations and side reactions in the precursor solution or during the evaporation of the residual solvent in the films which is detrimental to the solution stability, perovskite phase, and device performance.[16-19] To improve the long-term stability of efficient PSCs, new strategies that reduce the amount of DMSO are needed, without compromising performance.

The perovskite precursor solution composition and concentration also have a significant influence on the properties of the perovskite layer. For instance, the ratio of each precursor affects the final perovskite composition, bandgap, and crystallographic structure. In addition, quality of the perovskite films is greatly affected by iodoplumbate species that result from coordination of Pb and solvent molecules in the solution,[20-23] and intermediate phases such as PbI$_2$-(DMSO)$_x$, MAI-PbI$_2$-(DMSO)$_x$ (MA denotes methylammonium), and FAI-PbI$_2$-(DMSO)$_x$.[7,24-32] Since the intermediate phase, or at least its concentration, is determined by the ratio and amounts of perovskite and liquid additives, reducing the molarity of the perovskite precursor solution can reduce not only the coordinated and intermediate species, but also the concentration of DMSO needed to prepare the solution. Although iodoplumbate species vary with perovskite precursor concentration,[33] various concentrations and compositions of perovskite solutions with Pb:DMSO molar ratios of 1.0:1.0~1.5 are commonplace for high-performance PSCs.[3,8,10,12,29] However, reducing molarity, on its own, also reduces the thickness of the perovskite layer toward those unable to harvest a sufficient fraction of above-bandgap sunlight.

The process of hot-casting, whereby a heated substrate is used during film processing, has shown that perovskite film thickness increases on elevated temperature substrates due to a higher density of heterogeneous nuclei.[34-36] In addition, hot-casting can possess several advantages. For example, it has been reported that mild hot-casting at 55 °C can lower the post-deposition annealing temperature of all-inorganic $CsPbI_2Br$ perovskite layers significantly without compromising film quality.[37] Chang *et al.* reported that substrate temperature higher than 100 °C changes the formation mechanism of $MAPbI_{3-x}Cl_x$ films from one of multistage formation to a direct formation mechanism which resulted in larger grain size, and improved power conversion efficiency (PCE).[38] Zhang *et al.* reported that this direct formation enables high quality $(BA)_2(MA)_3Pb_4I_{13}$ (BA denotes butylammonium) films with preferentially perpendicular quantum well orientation, high phase purity, and improved optoelectronic properties.[39] Furthermore, hot-casting can reduce the amount of residual solvents by promoting its evaporation during the spin-coating process.[39-42]

Here we report PSCs with improved stability by reducing the concentration of DMSO and perovskite precursors, while maintaining the thickness of perovskite films through hot-casting deposition. We observe that the morphology and crystallinity of the $FAPbI_3$ films are highly dependent on the ratio of $FAPbI_3$-DMSO in the precursor solution. By reducing the concentration of perovskite precursors by half, we can reduce the amount of DMSO in precursor solution by quadruple without compromising the quality of the films – both morphologically and optoelectronically - improving PCE by suppressing nonradiative recombination at the perovskite-substrate interface where most generation occurs. The residual amount of DMSO in as-spin-coated films was reduced significantly, by a factor of 30, due to the combined effect of hot-casting and reduced initial amount of DMSO. As a result, we achieved a PCE of 23.4% (23.0% stabilized efficiency) with improved long-term stability by suppressing the formation of undesired impurity phases which are often the trigger for PSC

degradation.[15,43-45]

We solution-processed various concentrations of FAPbI$_3$ with 3.8 mol% methylenediammonium dichloride (MDACl$_2$) as an α-phase stabilizer[14] and 35 mol% methylammonium chloride (MACl) as a mediator[46] for preferred orientation and uniform morphology on indium-tin-oxide-(ITO-)coated glass and evaluated dependence of thickness on hot-casting temperature, as shown in Figure 1a. In general, without hot-casting, spin-coating using anti-solvent quenching[1] with 1.40 M FAPbI$_3$ yields a thickness of approximately 500 nm.[8-9,14] We observed a thickness of 475 nm with 1.40 M (representative film profile shown in Figure S1), and thicknesses of 220, 129, and 71 nm with FAPbI$_3$ concentrations of 0.74, 0.50, and 0.38 M, respectively. The thicknesses of perovskite layers were consistent across multiple measurements on multiple films processed with similar conditions, showing ±5% standard deviation (Table S1). The thickness of the perovskite layer increases with hot-casting temperature, similar to a previous report.[34-36] Notably for our ability to make meaningful comparisons, thicknesses of 482 and 499 nm are obtained with 0.74 M at 75 °C, and 0.50 M at 120 °C, respectively, values similar to films prepared with a 1.40 M ink and a room-temperature (RT, 25 °C) substrate.

We analyzed X-ray diffraction (XRD) patterns of as-annealed 1.40 M-RT, 0.74 M-75 °C, and 0.50 M-120 °C perovskite films, which have similar thickness, depending on the DMF:DMSO volume ratio (Figure 1b). All perovskite layers showed only phase pure α-phase of FAPbI$_3$ with two dominant peaks near 14° and 28°, which can be assigned to the α(100) and α(200) crystal planes, respectively. In general, well-oriented and textured films with strong XRD peaks indicate that it may facilitate charge transport and extraction. And despite similar film thicknesses, differences in the XRD patterns are apparent. When we reduce the amount of DMSO from 1.40 M FAPbI$_3$ dissolved in DMF:DMSO (8:1 volume ratio) (denoted as 1.40 M

(8:1)) to DMF:DMSO (16:1 volume ratio) (denoted as 1.40 M (16:1)), the XRD peak intensity was decreased. By contrast, 0.74 M in DMF:DMSO (16:1 volume ratio) (denoted as 0.74 M (16:1)), and 0.50 M in DMF:DMSO (24:1 volume ratio) (denoted as 0.50 M (24:1)) showed higher XRD peak intensity than 0.74 M in DMF:DMSO (8:1 volume ratio) (denoted as 0.74 M (8:1)), and 0.50 M in DMF:DMSO (8:1 volume ratio) (denoted as 0.50 M (8:1)), respectively. In addition, 0.74 M (16:1) and 0.50 M (24:1) showed a lower full width at half maximum (FWHM) for the (100) diffraction peak than 0.74 M (8:1) and 0.50 M (8:1), which indicates increased crystallite size (Figure 1c). In terms of the ratio of FAPbI$_3$ and DMSO in the precursor solution, 1.40 M (8:1), 0.74 M (16:1), and 0.50 M (24:1) are identical, which is FAPbI$_3$:DMSO (1:1.11 molar ratio). In addition, the hot-casting temperature does not have a significant effect on the crystallinity of the FAPbI$_3$ films within this range (Figure S2a-d). These results imply that the ratio of FAPbI$_3$ and DMSO has a greater influence on crystallinity of films than the hot-casting temperature. Additionally, we determined that neither hot-casting nor the DMSO ratio modify the bandgap of the FAPbI$_3$ layer, as ultraviolet-visible (UV-vis) absorption spectra (Figure S3) of films were nearly identical.

Figure 1d displays top-view scanning electron microscope (SEM) images of FAPbI$_3$ layers prepared with 1.40 M (8:1), 1.40 M (16:1), 0.74 M (16:1), and 0.50 M (24:1). The high Gutmann's donor number (D_N) solvent, DMSO, coordinates strongly with the Pb^{2+} center.[47] This means that DMSO inhibits iodide coordination and stalls perovskite crystallization but leads to improved film morphology. A uniform and almost pinhole-free surface was observed in 1.40 M (8:1) as reported previously.[9,13-14] However, 1.40 M (16:1) showed relatively poor morphology with many pinholes owing to an insufficient amount of DMSO. Despite the small amount of DMSO, a uniform and almost pinhole-free surface was observed with 0.74 M (16:1), and 0.50 M (24:1) similar to 1.4 M (8:1). This provides additional confirmation that the properties of the perovskite film are highly dependent on the perovskite-liquid additive ratio,

6

rather than the ratio of the main solvent-liquid additive.

Figure 2a shows the PCE distribution of the PSCs fabricated using 1.40 M (8:1), 0.74 M (16:1), and 0.50 M (24:1) perovskite layers. The device structure consisted of ITO/SnO$_2$/perovskite/*2,2',7,7'*-tetrakis[*N,N*-di(4methoxyphenyl)amino]-*9,9'*-spirobifluorene (Spiro-OMeTAD)/Au. The average PCE of 15 devices fabricated using 1.40 M (8:1), 0.74 M (16:1), and 0.50 M (24:1) perovskite layers are 21.7 ± 0.4%, 22.2 ± 0.6%, and 21.6 ± 0.8%, respectively. The PCE improvement from 1.40 M (8:1) to 0.74 M (16:1) was mainly owing to an increase in the open-circuit voltage (V_{OC}) (Figure S4a-c). We ascribe the lower PCE with broader distribution of the 0.50 M (24:1) to the nonuniform perovskite film formation during anti-solvent quenching at hot-casting temperatures of 120 °C or higher (Figure S5).

The current density-voltage (*J-V*) characteristics, reverse and forward bias sweep, for the best-performing devices prepared from 1.40 M (8:1) and 0.74 M (16:1) are depicted in Figure 2b. The PCE obtained from the *J-V* curve of 1.40 M (8:1) and 0.74 M (16:1) devices were 22.6%, and 23.4%, respectively, with about 1.0~1.5% absolute efficiency of hysteresis (Table S2). We measured the steady-state power output (SPO) of 1.40 M (8:1) and 0.74 M (8:1) devices for 250 s at a fixed voltage near the maximum power point (MPP) obtained from the peak *J-V* curves (Figure 2c). Devices prepared with 1.40 M (8:1) and 0.74 M (16:1) showed stable output within this range, with 21.7%, and 23.0%, respectively, which are nearly intermediate to that obtained from the reverse and forward scans. The integrated short-circuit current density (J_{SC}) calculated from the external quantum efficiency (EQE) of 0.74 M (16:1) (23.81 mA cm^{-2}) were slightly higher than that of 1.40 M (8:1) (23.53 mA cm^{-2}) (Figure 2d), consistent with the *J-V* characteristics (Figure S4a). In addition, cross-sectional images of devices prepared with 1.40 M (8:1) and 0.74 M (16:1) showed no significant difference in the thickness of each layer (Figure S6).

The PCE improvement from 1.40 M (8:1) to 0.74 M (16:1) can be attributed to a lower trap density, particularly at the perovskite-substrate interface where most charge photogeneration occurs, because residual DMSO can be trapped at the perovskite-substrate interface rather than the perovskite surface.[15] Additionally, during the spin-coating process, hot-casting can affect the residual amount of DMSO contained in the films. To investigate the amount of residual DMSO during the process, we immersed the perovskite films in deuterium oxide (D_2O) and then performed proton nuclear magnetic resonance (^{1}H-NMR) characterization. By comparing the integrated area of DMSO ^{1}H-NMR peak (2.61 ppm) and that of FA (7.68 ppm), we could quantify the relative amount of DMSO to FA. Figure 3a, b display ^{1}H-NMR signals of FA and DMSO obtained from 1.40 M (8:1) and 0.74 M (16:1) perovskite films without annealing. For ^{1}H-NMR, we normalized the integration area of proton around the C atom in FA. Interestingly, the amount of DMSO in the precursor solution of 1.40 M (8:1) only quadruple compared to 0.74 M (16:1), but right after the spin-coating process, the difference was more than 30 times. The ratio of DMSO to FA was 23:1 for 1.40 M (8:1) and 0.74:1 for 0.74 M (16:1). It can be speculated that this is because hot-casting promote evaporation of solvents including DMSO, that is otherwise trapped in disordered solvate phases, during the spin-coating process.[39-42] During the annealing process at 120 °C, 0.74 M (16:1) films continuously showed a lower amount of residual DMSO than 1.40 M (8:1) (Figure 3c, and Figure S7a, b).

The residual DMSO in the film can promote the side reaction between MA and FA by facilitating the proton transfer due to its relatively strong Lewis base behavior, forming byproducts such as N-methyl formamidinium iodide (MFAI) and N,N'-dimethyl formamidium iodide (DMFAI) during the annealing process.[16] Such side reactions yield impurity phases with insulating characteristics and thus limit charge-carrier generation and transport. Figure 3d-f depicts magnified ^{1}H-NMR spectra of 1.40 M (8:1) and 0.74 M (16:1) depending on annealing conditions in the region that byproduct signals appear. Before annealing, both 1.40

8

M (8:1) and 0.74 M (16:1) showed no byproducts (Figure 3d). However, after annealing at 120 °C for 1 min, 1.40 M (8:1) showed a proton signal near 2.80 ppm, which is a signal from MFAI (Figure 3e).[16] After annealing at 120 °C for 40 min, the peak of MFAI is more clearly observed in 1.40 M (8:1) while only a trace amount of it is observed in 0.74 M (16:1) (Figure 3f). In addition, we observed considerable NMR signal of the byproducts from both 1.40 M (8:1) and 0.74 M (16:1) after annealing at 150 °C for 10 min (Figure S8), which is consistent with previously reported results that these side reactions are highly dependent on temperature.[16] The small amount of the undesired reaction byproducts due to the small amount of residual DMSO in the 0.74 M (16:1) in our perovskite film annealing condition (120 °C) may allow for more phase pure and low defect density FAPbI$_3$ layers.

We conducted steady-state photoluminescence (PL), with a relatively short wavelength excitation source, from the substrate (bottom) and perovskite (top) sides to investigate the impact of residual DMSO and their byproducts on the perovskite surface and interface with the substrate. By estimating the absorption coefficient (α) of our perovskite layer from UV-vis absorption spectra (Figure S9a), we were able to calculate the penetration depth at each excitation wavelength according to $F(x) = F(x_0)e^{-\alpha(x-x_0)}$, where $F(x)$ is the intensity at a point x below the surface of the layer, and $F(x_0)$ is the intensity at the surface x_0. The 450 and 375 nm excitation penetrates approximately 35 and 20 nm into the perovskite layer, respectively (Figure S9b). In addition, absorption at these wavelengths by the substrate is negligible (Figure S9c). Figure 4a depicts steady-state PL spectra from the perovskite side using 450 nm excitation. Perovskite films prepared with 0.74 M (16:1) showed higher PL intensity than 1.40 M (8:1), but the difference was not significant. However, differences in PL intensity between 1.40 M (8:1) and 0.74 M (16:1) films were notable at the substrate side. With the same excitation, 450 nm, 0.74 M (16:1) showed approximately twice higher PL intensity

compared to 1.40 M (8:1) films (Figure 4b). The PL intensity difference between 1.40 M (8:1) and 0.74 M (16:1) films was even more pronounced when we used the smaller penetration depth, 375 nm excitation source (Figure 4c). This result is consistent with previous reports that residual DMSO is predominantly at the buried perovskite-substrate interface,[15] increasing defect density.[48] Furthermore, we derived the Urbach energy (E_u) (Figure S10) of 1.40 M (8:1) and 0.74 M (16:1) from EQE spectra (Figure 2d). Given the almost similar reflectance of the devices, E_u can be expressed by $ln(EQE) = C + hv/E_u$, where C and hv are a constant and photon energy, respectively. The smaller E_u value indicates higher optoelectronic quality and minimal voltage deficiency. The E_u of the 1.40 M (8:1) device was 15.5 meV, whereas it was 14.7 meV for the 0.74 M (16:1) device. The reduced Urbach energy is consistent with the V_{OC} improvement of 0.74 M (16:1) devices compared to 1.40 M (8:1).

Figure 5a shows the PCE stability of 5 devices each of 1.40 M (8:1) and 0.74 M (16:1) which were stored at 15 to 30% relative humidity (RH) under dark and ambient air conditions. Devices prepared with 0.74 M (16:1) showed a narrower distribution compared to 1.40 M (8:1), but all devices showed no significant PCE degradation. We then performed maximum power point tracking (MPPT) to quantify the operational stability of encapsulated 1.40 M (8:1) and 0.74 M (16:1) devices at ambient conditions (30 °C, 35% RH) under continuous illumination using a metal-halide lamp. This lamp possesses 2.6 times higher power density in the UV-region (300-400 nm) compared to the AM 1.5G spectrum with an overall power density of 1.1 sun (Figure S11, Table S3).[49] As an anti-reflection film is attached[9] on our devices without a UV cut-off filter, the test is more overall-power- and UV-intense than an MPPT test using either Xenon lamp or white light emitting diode (LED) illumination.[50-51] As shown in Figure 5b, at this intense UV-containing light soaking, the PCE of both 1.40 M (8:1), and 0.74 M (16:1) device decreased rapidly by <25%, and <15% of its initial efficiency in the initial ~5 h, respectively (the initial *J-V* curves and device parameters are presented in Figure S12). The initial rapid

burn-in effect has been observed in various perovskite compositions, device structures, and even in organic photovoltaics.[52-56] Although the exact nature of the burn-in effect in PSCs is still under debate, it has been previously ascribed to the ion migration or the contact-layer interface.[52-53] In addition, initial burn-in and second decay rate are highly dependent on the operating conditions such as atmosphere, encapsulation, and UV-contents of the light source.[57] We determined the initial burn-in region as ~5 h using a linear model (coefficient of determination $R^2 > 83\%$). After the rapid initial burn-in, the devices showed much slower secondary linear decay, similar to previous reports.[52-55] Devices prepared with 0.74 M (16:1) showed less initial burn-in and much slower secondary decay (-0.84% of initial efficiency per 100 h) than 1.40 M (8:1) (-1.89% of initial efficiency per 100 h) (Figure S13). As a result, 0.74 M (16:1) devices maintained over 80% and 93% of PCE while 1.40 M (8:1) retained 60% and 85% of its initial and post-burn-in PCE over 800 h, respectively. We ascribe the improved operational stability under high-power of UV-containing illumination of 0.74 M (16:1) devices compared with 1.40 (8:1) to fewer defects at the perovskite-substrate interface, because UV-light with a short-wavelength (<400 nm) can only penetrate 10-20 nm into the perovskite layer (Figure S9) and it is already reported that operational stability under UV-containing illumination is highly dependent on the perovskite-substrate interface.[8,14,58]

In summary, we observed that surface morphology and the crystallinity including crystallite size and orientation are highly dependent on the FAPbI$_3$:DMSO ratio in the precursor solution. To reduce the residual amount of DMSO in films, which can initiate the side reaction with and induce defects at the perovskite-substrate interface, we used hot-casting to reduce the initial amount of DMSO without compromising perovskite film thickness. Hot-casting allowed for reducing the amount of DMSO in the ink by a factor of 4 and promoted removal of DMSO during the process, which led to significantly reduced residual DMSO in films by a factor of 30. Reducing the amount of residual DMSO in the films effectively suppressed the formation

of the undesired reaction byproducts which resulted in superior PCE and stability. Consequently, we were able to manufacture PSCs with a PCE of 23.4% (23.0% stabilized efficiency), with high operational stability under high-power of UV-containing continuous illumination (overall power density of 1.1 sun with 2.6 times higher UV-region power density than AM 1.5G) maintaining over 80% and 93% of its initial and post-burn-in PCE after 800 h.

Supporting Information

Supporting Information is available from the Wiley Online Library or from the author.

Acknowledgements

Conflict of Interest

The authors declare no conflict of interest.

Author Contributions

H.M. conceived this work and designed the experiment. H.M. fabricated the PSCs and

characterized the perovskite films. J.H. measured XRD patterns and NMR. Z.X. carried out SEM and PL measurements. T.L. conducted MPPT with supervision from Y-L.L. S-U-Z. K. measured EQE. K.R. conducted profilometer. H.M. and B.P.R. wrote the draft of the manuscript, and all authors contributed feedback and comments for revising the manuscript. B.P.R. supervised the study.

Data Availability Statement

Research data are not shared.

Keywords

Perovskite solar cells, hot-casting, dimethyl sulfoxide, UV-stability, perovskite-substrate interface

References

[1]   N. J. Jeon, J. H. Noh, Y. C. Kim, W. S. Yang, S. Ryu, S. I. Seok, *Nature Materials* **2014**, 13, 897.
[2]   N. J. Jeon, J. H. Noh, W. S. Yang, Y. C. Kim, S. Ryu, J. Seo, S. I. Seok, *Nature* **2015**, 517, 476.
[3]   J.-W. Lee, Z. Dai, C. Lee, H. M. Lee, T.-H. Han, N. De Marco, O. Lin, C. S. Choi, B. Dunn, J. Koh, D. Di Carlo, J. H. Ko, H. D. Maynard, Y. Yang, *Journal of the American Chemical Society* **2018**, 140, 6317.
[4]   X. Fang, Y. Wu, Y. Lu, Y. Sun, S. Zhang, J. Zhang, W. Zhang, N. Yuan, J. Ding, *Journal of Materials Chemistry C* **2017**, 5, 842.
[5]   J. Li, J. Dagar, O. Shargaieva, M. A. Flatken, H. Köbler, M. Fenske, C. Schultz, B. Stegemann, J. Just, D. M. Többens, A. Abate, R. Munir, E. Unger, *Advanced Energy Materials* **2021**, 11, 2003460.
[6]   B. Conings, A. Babayigit, M. T. Klug, S. Bai, N. Gauquelin, N. Sakai, J. T.-W. Wang, J. Verbeeck, H.-G. Boyen, H. J. Snaith, *Advanced Materials* **2016**, 28, 10701.
[7]   Y. Rong, Z. Tang, Y. Zhao, X. Zhong, S. Venkatesan, H. Graham, M. Patton, Y. Jing, A. M. Guloy, Y. Yao, *Nanoscale* **2015**, 7, 10595.
[8]   H. Min, D. Y. Lee, J. Kim, G. Kim, K. S. Lee, J. Kim, M. J. Paik, Y. K. Kim, K. S. Kim, M. G. Kim, T. J. Shin, S. Il Seok, *Nature* **2021**, 598, 444.
[9]   G. Kim, H. Min, K. S. Lee, D. Y. Lee, S. M. Yoon, S. I. Seok, *Science* **2020**, 370, 108.
[10]   J. Jeong, M. Kim, J. Seo, H. Lu, P. Ahlawat, A. Mishra, Y. Yang, M. A. Hope, F. T. Eickemeyer, M. Kim, Y. J. Yoon, I. W. Choi, B. P. Darwich, S. J. Choi, Y. Jo, J. H. Lee, B. Walker, S. M. Zakeeruddin, L. Emsley, U. Rothlisberger, A. Hagfeldt, D. S. Kim, M. Grätzel, J. Y. Kim, *Nature* **2021**, 592, 381.
[11]   M. Kim, J. Jeong, H. Lu, T. K. Lee, F. T. Eickemeyer, Y. Liu, I. W. Choi, S. J. Choi, Y. Jo, H.-B. Kim, S.-I. Mo, Y.-K. Kim, H. Lee, N. G. An, S. Cho, W. R. Tress, S. M. Zakeeruddin, A. Hagfeldt, J. Y. Kim, M. Grätzel, D. S. Kim, *Science* **2022**, 375, 302.
[12]   J. J. Yoo, G. Seo, M. R. Chua, T. G. Park, Y. Lu, F. Rotermund, Y.-K. Kim, C. S. Moon, N. J. Jeon, J.-P. Correa-Baena, V. Bulović, S. S. Shin, M. G. Bawendi, J. Seo, *Nature* **2021**, 590, 587.
[13]   Y.-W. Jang, S. Lee, K. M. Yeom, K. Jeong, K. Choi, M. Choi, J. H. Noh, *Nature Energy* **2021**, 6, 63.
[14]   H. Min, M. Kim, S.-U. Lee, H. Kim, G. Kim, K. Choi, J. H. Lee, S. I. Seok, *Science* **2019**, 366, 749.
[15]   S. Chen, X. Dai, S. Xu, H. Jiao, L. Zhao, J. Huang, *Science* **2021**, 373, 902.
[16]   R. Liu, Z. Li, C. Chen, Y. Rao, X. Sun, L. Wang, X. Wang, Z. Zhou, T. Jiu, X. Guo, S. Frank Liu, S. Pang, *ACS Applied Materials & Interfaces* **2020**, 12, 35043.

[17]   J. C. Hamill, J. C. Sorli, I. Pelczer, J. Schwartz, Y.-L. Loo, *Chemistry of Materials* **2019**, 31, 2114.
[18]   H. Min, G. Kim, M. J. Paik, S. Lee, W. S. Yang, M. Jung, S. I. Seok, *Advanced Energy Materials* **2019**, 9, 1803476.
[19]   P. K. Nayak, D. T. Moore, B. Wenger, S. Nayak, A. A. Haghighirad, A. Fineberg, N. K. Noel, O. G. Reid, G. Rumbles, P. Kukura, K. A. Vincent, H. J. Snaith, *Nature Communications* **2016**, 7, 13303.
[20]   E. Radicchi, E. Mosconi, F. Elisei, F. Nunzi, F. De Angelis, *ACS Applied Energy Materials* **2019**, 2, 3400.
[21]   R. Munir, A. D. Sheikh, M. Abdelsamie, H. Hu, L. Yu, K. Zhao, T. Kim, O. E. Tall, R. Li, D.-M. Smilgies, A. Amassian, *Advanced Materials* **2017**, 29, 1604113.
[22]   A. Sharenko, C. Mackeen, L. Jewell, F. Bridges, M. F. Toney, *Chemistry of Materials* **2017**, 29, 1315.
[23]   K. Yan, M. Long, T. Zhang, Z. Wei, H. Chen, S. Yang, J. Xu, *Journal of the American Chemical Society* **2015**, 137, 4460.
[24]   S. I. Seok, M. Grätzel, N.-G. Park, *Small* **2018**, 14, 1704177.
[25]   N. Ahn, D.-Y. Son, I.-H. Jang, S. M. Kang, M. Choi, N.-G. Park, *Journal of the American Chemical Society* **2015**, 137, 8696.
[26]   W. S. Yang, J. H. Noh, N. J. Jeon, Y. C. Kim, S. Ryu, J. Seo, S. I. Seok, *Science* **2015**, 348, 1234.
[27]   M. Wang, F. Cao, K. Deng, L. Li, *Nano Energy* **2019**, 63, 103867.
[28]   Y. Bai, S. Xiao, C. Hu, T. Zhang, X. Meng, Q. Li, Y. Yang, K. S. Wong, H. Chen, S. Yang, *Nano Energy* **2017**, 34, 58.
[29]   J. Cao, X. Jing, J. Yan, C. Hu, R. Chen, J. Yin, J. Li, N. Zheng, *Journal of the American Chemical Society* **2016**, 138, 9919.
[30]   Q. Hu, L. Zhao, J. Wu, K. Gao, D. Luo, Y. Jiang, Z. Zhang, C. Zhu, E. Schaible, A. Hexemer, C. Wang, Y. Liu, W. Zhang, M. Grätzel, F. Liu, T. P. Russell, R. Zhu, Q. Gong, *Nature Communications* **2017**, 8, 15688.
[31]   Z.-w. Kwang, C.-W. Chang, T.-Y. Hsieh, T.-C. Wei, S.-Y. Lu, *Electrochimica Acta* **2018**, 266, 118.
[32]   P. P. Khlyabich, Y.-L. Loo, *Chemistry of Materials* **2016**, 28, 9041.
[33]   A. M. Valencia, O. Shargaieva, R. Schier, E. Unger, C. Cocchi, *The Journal of Physical Chemistry Letters* **2021**, 12, 2299.
[34]   J. Chen, L. Zuo, Y. Zhang, X. Lian, W. Fu, J. Yan, J. Li, G. Wu, C.-Z. Li, H. Chen, *Advanced Energy Materials* **2018**, 8, 1800438.
[35]   S. Hu, X. Yang, B. Yang, Y. Zhang, H. Li, C. Sheng, *The Journal of Physical Chemistry C* **2021**, 125, 2212.
[36]   C. Zuo, A. D. Scully, D. Vak, W. Tan, X. Jiao, C. R. McNeill, D. Angmo, L. Ding, M. Gao, *Advanced Energy Materials* **2019**, 9, 1803258.
[37]   Z. Wang, X. Liu, Y. Lin, Y. Liao, Q. Wei, H. Chen, J. Qiu, Y. Chen, Y. Zheng, *Journal of Materials Chemistry A* **2019**, 7, 2773.
[38]   C.-Y. Chang, Y.-C. Huang, C.-S. Tsao, W.-F. Su, *ACS Applied Materials & Interfaces* **2016**, 8, 26712.
[39]   X. Zhang, R. Munir, Z. Xu, Y. Liu, H. Tsai, W. Nie, J. Li, T. Niu, D.-M. Smilgies, M. G. Kanatzidis, A. D. Mohite, K. Zhao, A. Amassian, S. Liu, *Advanced Materials* **2018**, 30, 1707166.
[40]   Y. Fan, J. Fang, X. Chang, M.-C. Tang, D. Barrit, Z. Xu, Z. Jiang, J. Wen, H. Zhao, T. Niu, D.-M. Smilgies, S. Jin, Z. Liu, E. Q. Li, A. Amassian, S. Liu, K. Zhao, *Joule* **2019**, 3, 2485.
[41]   S. Tang, Y. Deng, X. Zheng, Y. Bai, Y. Fang, Q. Dong, H. Wei, J. Huang, *Advanced Energy Materials* **2017**, 7, 1700302.
[42]   J. J. van Franeker, K. H. Hendriks, B. J. Bruijnaers, M. W. G. M. Verhoeven, M. M. Wienk, R. A. J. Janssen, *Advanced Energy Materials* **2017**, 7, 1601822.
[43]   J. S. Yun, J. Kim, T. Young, R. J. Patterson, D. Kim, J. Seidel, S. Lim, M. A. Green, S. Huang, A. Ho-Baillie, *Advanced Functional Materials* **2018**, 28, 1705363.
[44]   G. Tumen-Ulzii, C. Qin, D. Klotz, M. R. Leyden, P. Wang, M. Auffray, T. Fujihara, T. Matsushima, J.-W. Lee, S.-J. Lee, Y. Yang, C. Adachi, *Advanced Materials* **2020**, 32, 1905035.
[45]   G. Tong, D.-Y. Son, L. K. Ono, H.-B. Kang, S. He, L. Qiu, H. Zhang, Y. Liu, J. Hieulle, Y. Qi, *Nano Energy* **2021**, 87, 106152.
[46]   M. Kim, G.-H. Kim, T. K. Lee, I. W. Choi, H. W. Choi, Y. Jo, Y. J. Yoon, J. W. Kim, J. Lee, D. Huh, H. Lee, S. K. Kwak, J. Y. Kim, D. S. Kim, *Joule* **2019**, 3, 2179.
[47]   J. C. Hamill, J. Schwartz, Y.-L. Loo, *ACS Energy Letters* **2018**, 3, 92.
[48]   F. Zhang, J. C. Hamill Jr., Y.-L. Loo, A. Kahn, *Advanced Materials* **2020**, 32, 2003482.
[49]   X. Zhao, T. Liu, A. B. Kaplan, C. Yao, Y.-L. Loo, *Nano Letters* **2020**, 20, 8880.
[50]   I. Mathews, G. Kelly, P. J. King, R. Frizzell, presented at *2014 IEEE 40th Photovoltaic Specialist Conference (PVSC)*, 8-13 June 2014, **2014**.
[51]   G. Leary, G. Switzer, G. Kuntz, T. Kaiser, presented at *2016 IEEE 43rd Photovoltaic Specialists Conference (PVSC)*, 5-10 June 2016, **2016**.

[52]   K. Domanski, B. Roose, T. Matsui, M. Saliba, S.-H. Turren-Cruz, J.-P. Correa-Baena, C. R. Carmona, G. Richardson, J. M. Foster, F. De Angelis, J. M. Ball, A. Petrozza, N. Mine, M. K. Nazeeruddin, W. Tress, M. Grätzel, U. Steiner, A. Hagfeldt, A. Abate, *Energy & Environmental Science* **2017**, 10, 604.

[53]   J. A. Christians, P. Schulz, J. S. Tinkham, T. H. Schloemer, S. P. Harvey, B. J. Tremolet de Villers, A. Sellinger, J. J. Berry, J. M. Luther, *Nature Energy* **2018**, 3, 68.

[54]   M. V. Khenkin, E. A. Katz, A. Abate, G. Bardizza, J. J. Berry, C. Brabec, F. Brunetti, V. Bulović, Q. Burlingame, A. Di Carlo, R. Cheacharoen, Y.-B. Cheng, A. Colsmann, S. Cros, K. Domanski, M. Dusza, C. J. Fell, S. R. Forrest, Y. Galagan, D. Di Girolamo, M. Grätzel, A. Hagfeldt, E. von Hauff, H. Hoppe, J. Kettle, H. Köbler, M. S. Leite, S. Liu, Y.-L. Loo, J. M. Luther, C.-Q. Ma, M. Madsen, M. Manceau, M. Matheron, M. McGehee, R. Meitzner, M. K. Nazeeruddin, A. F. Nogueira, Ç. Odabaşı, A. Osherov, N.-G. Park, M. O. Reese, F. De Rossi, M. Saliba, U. S. Schubert, H. J. Snaith, S. D. Stranks, W. Tress, P. A. Troshin, V. Turkovic, S. Veenstra, I. Visoly-Fisher, A. Walsh, T. Watson, H. Xie, R. Yıldırım, S. M. Zakeeruddin, K. Zhu, M. Lira-Cantu, *Nature Energy* **2020**, 5, 35.

[55]   Y.-H. Lin, N. Sakai, P. Da, J. Wu, H. C. Sansom, A. J. Ramadan, S. Mahesh, J. Liu, R. D. J. Oliver, J. Lim, L. Aspitarte, K. Sharma, P. K. Madhu, A. B. Morales-Vilches, P. K. Nayak, S. Bai, F. Gao, C. R. M. Grovenor, M. B. Johnston, J. G. Labram, J. R. Durrant, J. M. Ball, B. Wenger, B. Stannowski, H. J. Snaith, *Science* **2020**, 369, 96.

[56]   R. Roesch, T. Faber, E. von Hauff, T. M. Brown, M. Lira-Cantu, H. Hoppe, *Advanced Energy Materials* **2015**, 5, 1501407.

[57]   K. Domanski, E. A. Alharbi, A. Hagfeldt, M. Grätzel, W. Tress, *Nature Energy* **2018**, 3, 61.

[58]   H. Tan, A. Jain, O. Voznyy, X. Lan, F. P. G. d. Arquer, J. Z. Fan, R. Quintero-Bermudez, M. Yuan, B. Zhang, Y. Zhao, F. Fan, P. Li, L. N. Quan, Y. Zhao, Z.-H. Lu, Z. Yang, S. Hoogland, E. H. Sargent, *Science* **2017**, 355, 722.
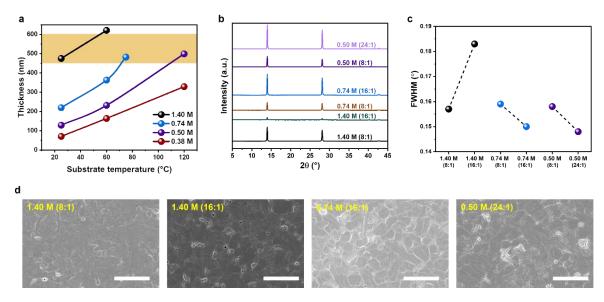
Figure 1. a) Thicknesses of perovskite films as a function of hot-casting (substrate) temperature for various perovskite concentrations. b) XRD patterns, c) FWHM of the (100) diffraction peak in Figure 1b, and d) SEM images of as-annealed perovskite films (all with ~500 nm thickness) prepared with different perovskite concentration and DMF:DMSO ratio. SEM scale bars are 5 μm.
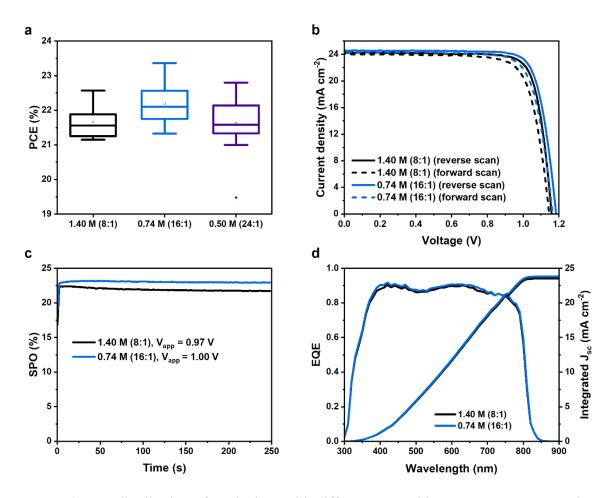
Figure 2. a) PCE distribution of 15 devices with different perovskite precursor concentrations (DMF:DMSO volume ratios): 1.40 M (8:1), 0.74 M (16:1), and 0.50 (24:1) (center line, median; small square, mean; box, 25-75% standard deviation; whiskers, outliers). b) *J-V* curves, c) steady-state power output with applied voltage (V_{app}), and d) EQE spectra and integrated JSC of 1.40 M (8:1), and 0.74 M (16:1) PSCs.
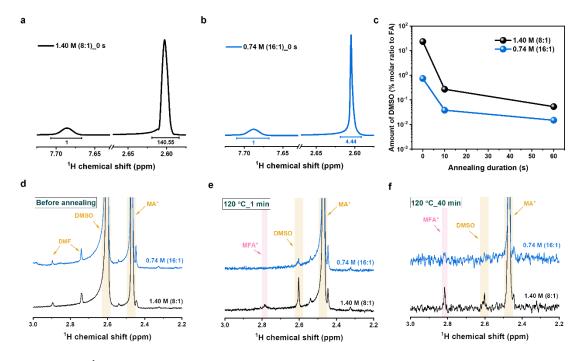
Figure 3. The ^{1}H-NMR signals of FA (7.68 ppm) and DMSO (2.61 ppm) obtained from as-spin-coated perovskite films prepared with a) 1.40 M (8:1) and b) 0.74 M (16:1) perovskite solution. c) The relative amount of DMSO to FA in the perovskite film vs. annealing duration determined from ^{1}H-NMR spectra of Figure 3a, b, S7a, and S7b. The ^{1}H-NMR spectra of the byproduct signals region depending on the annealing conditions, d) before annealing, e) at 120 ℃ for 1 min, and f) at 120 ℃ for 40 min.
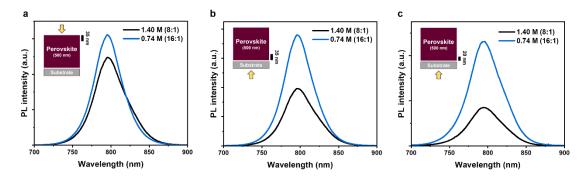
Figure 4. Steady-state PL spectra of 1.40 M (8:1) and 0.74 M (16:1) with different excitation wavelength and direction; a) 450 nm (perovskite-side), b) 450 nm (substrate-side), and c) 375 nm (substrate-side)
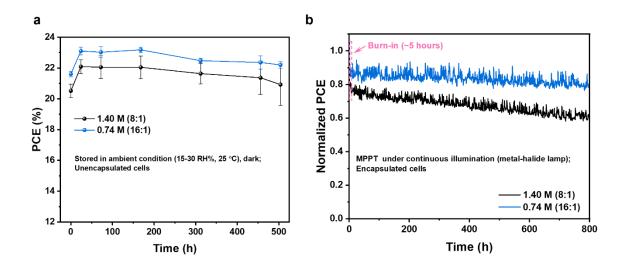
Figure 5. a) PCE monitored as a function of storage time of 5 unencapsulated 1.40 M (8:1) and 0.74 M (16:1) devices. The error bars denote standard deviation. b) Normalized PCE as a function of aging time of encapsulated 1.40 M (8:1) and 0.74 M (16:1) devices under continuous illumination (metal-halide lamp; overall power density of 1.1 sun with 2.6 times higher UV-region power density than AM 1.5G).